













# Artificial intelligence-guided design of lipid nanoparticles for pulmonary gene therapy

Received: 18 March 2024

Accepted: 29 October 2024

Published online: 10 December 2024

 Check for updates

Jacob Witten <sup>1,2,3,8</sup>, Idris Raji <sup>1,2,4,8</sup>, Rajith S. Manan <sup>1,2,8</sup>, Emily Beyer<sup>1</sup>, Sandra Bartlett<sup>1,2</sup>, Yinghua Tang<sup>5</sup>, Mehrnoosh Ebadi <sup>5</sup>, Junying Lei<sup>5</sup>, Dien Nguyen <sup>1,2</sup>, Favour Oladimeji<sup>2,3</sup>, Allen Yujie Jiang <sup>1,2</sup>, Elise MacDonald <sup>1,2</sup>, Yizong Hu<sup>1,2</sup>, Haseeb Mughal<sup>1,2</sup>, Ava Self<sup>1,2</sup>, Evan Collins <sup>2,3</sup>, Ziyang Yan <sup>5</sup>, John F. Engelhardt <sup>5</sup>, Robert Langer <sup>1,2,3,6,7</sup> & Daniel G. Anderson <sup>1,2,6,7</sup> ✉

Ionizable lipids are a key component of lipid nanoparticles, the leading nonviral messenger RNA delivery technology. Here, to advance the identification of ionizable lipids beyond current methods, which rely on experimental screening and/or rational design, we introduce lipid optimization using neural networks, a deep-learning strategy for ionizable lipid design. We created a dataset of >9,000 lipid nanoparticle activity measurements and used it to train a directed message-passing neural network for prediction of nucleic acid delivery with diverse lipid structures. Lipid optimization using neural networks predicted RNA delivery in vitro and in vivo and extrapolated to structures divergent from the training set. We evaluated 1.6 million lipids in silico and identified two structures, FO-32 and FO-35, with local mRNA delivery to the mouse muscle and nasal mucosa. FO-32 matched the state of the art for nebulized mRNA delivery to the mouse lung, and both FO-32 and FO-35 efficiently delivered mRNA to ferret lungs. Overall, this work shows the utility of deep learning for improving nanoparticle delivery.

Lipid nanoparticles (LNPs) for RNA delivery have recently begun to demonstrate their potential for improving human health<sup>1–3</sup>. Messenger RNA vaccines for coronavirus disease 2019 have provided exceptional protection against severe disease<sup>4,5</sup>, and hepatic RNA delivery has yielded the US Food and Drug Administration-approved Onpattro and other promising clinical programs<sup>1,6,7</sup>. Despite this, more potent and targeted LNPs are required to enable the broadest application of RNA therapies for genetic diseases, reduce side effects<sup>8</sup>, improve shelf stability<sup>9,10</sup>, deliver to extrahepatic tissue such as the lung epithelium<sup>11–14</sup> and improve control over inflammation<sup>15</sup>. Lung-targeted gene therapy

is particularly challenging<sup>14</sup> but has the potential to treat a range of diseases including cystic fibrosis (CF)<sup>14</sup>, idiopathic pulmonary fibrosis<sup>16–18</sup>, alpha-1 antitrypsin deficiency<sup>19</sup>, chronic obstructive pulmonary disease<sup>20</sup>, primary ciliary dyskinesia<sup>21</sup>, asthma<sup>22,23</sup> and more.

So far, ionizable lipids for LNP-based delivery have almost exclusively been designed via experimental screening, rational design<sup>24–26</sup> or a combination of the two<sup>15,27</sup>. Screens rely on high-yield combinatorial chemistry to generate chemically diverse lipid libraries, while rational design leverages features of potent ionizable lipids, such as biodegradable groups and branched tails<sup>24,25,27</sup>. More recently, an effort to use

<sup>1</sup>Department of Chemical Engineering, Massachusetts Institute of Technology, Cambridge, MA, USA. <sup>2</sup>David H. Koch Institute for Integrative Cancer Research, Massachusetts Institute of Technology, Cambridge, MA, USA. <sup>3</sup>Department of Biological Engineering, Massachusetts Institute of Technology, Cambridge, MA, USA. <sup>4</sup>Department of Anesthesiology, Boston Children's Hospital, Boston, MA, USA. <sup>5</sup>Department of Anatomy and Cell Biology, University of Iowa Carver College of Medicine, Iowa City, IA, USA. <sup>6</sup>Harvard and MIT Division of Health Science and Technology, Massachusetts Institute of Technology, Cambridge, MA, USA. <sup>7</sup>Institute for Medical Engineering and Science, Massachusetts Institute of Technology, Cambridge, MA, USA. <sup>8</sup>These authors contributed equally: Jacob Witten, Idris Raji, Rajith S. Manan. ✉e-mail: [dgander@mit.edu](mailto:dgander@mit.edu)

machine learning for LNPs has shown utility in designing analogs from a library of delivery lipids<sup>28</sup>.

Here, we introduce lipid optimization using neural networks (LiON), a deep learning (DL) approach for lipid discovery and design<sup>29–32</sup>. LiON uses deep message-passing neural networks (D-MPNNs), a subset of DL suitable for chemical structure analysis that has produced state-of-the-art performance<sup>30</sup> and assisted the identification of novel antibiotics<sup>29,33,34</sup>. We hypothesize that LiON could facilitate the design of potent lipids, including some that would not be deemed promising by human experts. Notably, in contrast to previous work<sup>28</sup> the power and flexibility of D-MPNNs allowed LiON to be trained on multiple chemically diverse libraries and learn generalizable rules about ionizable lipid design.

First, we used LiON to optimize the results from a previous bar-coded lipid library screen<sup>35</sup>, identifying an ionizable lipid RJ-A30-T01 that was nine times more potent for mRNA delivery than the top candidate from the previous screen and matched or exceeded top clinical<sup>1</sup> and preclinical<sup>24</sup> benchmarks for liver mRNA delivery.

Second, we used LiON to select ionizable lipid candidates synthesizable using a novel four-component reaction (4CR). Our top lipids, FO-32 and FO-35, yielded state-of-the-art mRNA delivery to the muscle, lung and nose. Moreover, FO-35 has a highly unique structure with little similarity to other published lipids. Taken together, these results show that DL can explore new regions of chemical space and yield substantial improvements in mRNA delivery potency.

Furthermore, both FO-32 and FO-35 LNPs enable potent transfection throughout the whole ferret lung epithelium, from trachea to alveoli. Ferrets are a widely used airway model due to strong physiological similarities with human airways<sup>36–38</sup>, and to our knowledge, the only reports in literature of successful ferret mRNA delivery have been polymeric nanoparticles that target the alveoli but not conducting airways<sup>39</sup>. Because the conducting airways are the critical site for muco-obstructive lung diseases, such as CF, chronic obstructive pulmonary disease and primary ciliary dyskinesia<sup>40</sup>, the widespread ferret lung epithelial targeting of FO-32 and FO-35 indicates substantial promise as pulmonary gene therapy agents.

## Results

### Dataset and DL model design

Our LiON approach has five steps. First, we collected all high-throughput LNP activity screens available to us both published and unpublished (Fig. 1a), which amounted to 20 unique datasets, including 4 in vivo screens with 575 individual datapoints and 16 in vitro with 8,727 individual datapoints<sup>15,28,41–49</sup> (Supplementary Table 1). Supplementary Fig. 1 illustrates the chemical diversity included in the dataset. Second, we used the dataset to train and evaluate a DL model for LNP potency prediction (Fig. 1b). Third, we used our model to predict mRNA delivery for all synthesizable ionizable lipids of a particular class (Fig. 1c). Fourth, we formulated and tested the top candidates in vivo (Fig. 1d). Lastly, we tested analogs of the top lipids to further optimize activity (Fig. 1e).

Because different datasets are incommensurable—one cannot, for example, reasonably compare mRNA delivery in HeLa cells<sup>15</sup> to barcoded liver mRNA delivery<sup>35</sup>—we report performance dataset by dataset below. Generating a standardized dataset in which multiple ionizable lipid libraries were screened under identical conditions, including cargo, target cell or tissue type and molar ratios and identities of helper lipids, would be a useful future endeavor, as would screening under multiple formulation conditions to allow the co-optimization of ionizable lipid and formulation. Here, we reasoned that despite screens having used different conditions and formulation parameters, LiON could, nevertheless, learn generalizable rules for ionizable lipid design. Because almost every screen varied lipid structure while holding formulation constant, we only optimized lipid structure, not formulation, with LiON.

### Design and characterization of the DL model for predicting LNP activity

LiON adapts D-MPNNs for the unique context of LNPs based on combinatorial chemistry-synthesized ionizable lipids. To make predictions, ionizable lipid structure and metadata (formulation, cargo and target information) are input into a D-MPNN from the Chemprop package<sup>50</sup>. Chemprop processes the lipid chemical structure with a D-MPNN and merges the D-MPNN output with the metadata in dense layers to output a single predicted quantity (Fig. 1b).

Following hyperparameter optimization, we trained the model using a 70%–15%–15% training–validation–test split and measured performance as the correlation coefficient between predicted and actual mRNA delivery activity for each individual dataset. We measured strong correlations across all datasets (Fig. 1f).

Because the lipids were generated using combinatorial chemistry, the datapoints are correlated, which makes the performance appear deceptively impressive and encourages overfitting (Supplementary Fig. 2a,b). Inspired by the use of scaffold-based splits in small molecule drug research<sup>51</sup>, we used a training–validation–test split based on amine headgroup (Supplementary Fig. 2c). Hence, performance is only measured on lipids with new amine headgroups for a particular dataset, reducing training–test correlation and forcing the model to extrapolate. Splitting on both amine and tail components would have required discarding a large fraction of the data (Supplementary Fig. 2d). As expected, performance was worse for the amine-based split, but we still observed near-universally significant positive correlations (Fig. 1g).

### Application of LiON to branched-ester library

For our first application of LiON, we sought to expand on a large in vivo dataset because accurate predictions would be more likely to translate to in vivo performance. Recently, our group reported a peptide-encoded barcoding approach to screen 384 branched-ester-containing lipids for liver mRNA delivery<sup>35</sup> (Fig. 2a). This study identified RM-133-3 as the top-performing lipid, along with an optimized formulation that we used for all of our experimental testing with this library. Our model performed well on this dataset (Fig. 1f,g).

We predicted liver mRNA delivery for a potential library of 2,574 lipids (Supplementary Tables 2 and 3). As shown by the top three predicted structures (Supplementary Fig. 3), the model preferred docosahexaenoic acid (DHA) and eicosapentaenoic acid (EPA) tails, as expected because the top 21 LNPs from the barcoded screen had DHA or EPA tails.

We examined lipids with EPA or DHA tails and the top 11 predicted headgroups for liver firefly luciferase (FFL) mRNA delivery, finding three candidates with comparable activity to RM-133-3 (Fig. 2b). The lipids with greater than three tails aggregated and had poor performance. RJ-A03-T16, a close RM-133-3 analog, was a slight improvement over RM-133-3 (Fig. 2c). Throughout this screening we generally used  $n = 1$  mouse/lipid to maximize throughput while minimizing use of mice, with occasional  $n = 2$  to confirm that our tests were reliable.

Next, we reasoned that the large DHA and EPA tails may not be optimal for the preferred larger headgroups. We, therefore, tested lipids with  $\alpha$ -linolenic acid (ALA) and  $\gamma$ -linolenic acid (GLA) tails, ranked third and fifth, ranked by the DL model (as measured by average predicted delivery across all headgroups) (Supplementary Table 4). As before, lipids with greater than or equal to four tails aggregated but RJ-A14-T30 and RJ-A14-T34 had promising delivery (Fig. 2d). Lipids with the fourth ranked arachidonic acid tail were worse than RJ-A14-T34 (Supplementary Fig. 4). RJ-A14-T34 was substantially more potent than DLin-MC3-DMA (MC3, approved for siRNA liver delivery as Onpatro<sup>1</sup>) and comparable with SM-102 (Moderna's US Food and Drug Administration-approved formulation for intramuscular coronavirus disease vaccination<sup>1</sup>), though less potent than lipid 5 (a liver-targeting candidate<sup>24</sup>) (Fig. 2e). Next, we tested the sixth ranked tail, identifying RJ-A30-T01, which was significantly more potent than both MC3 and

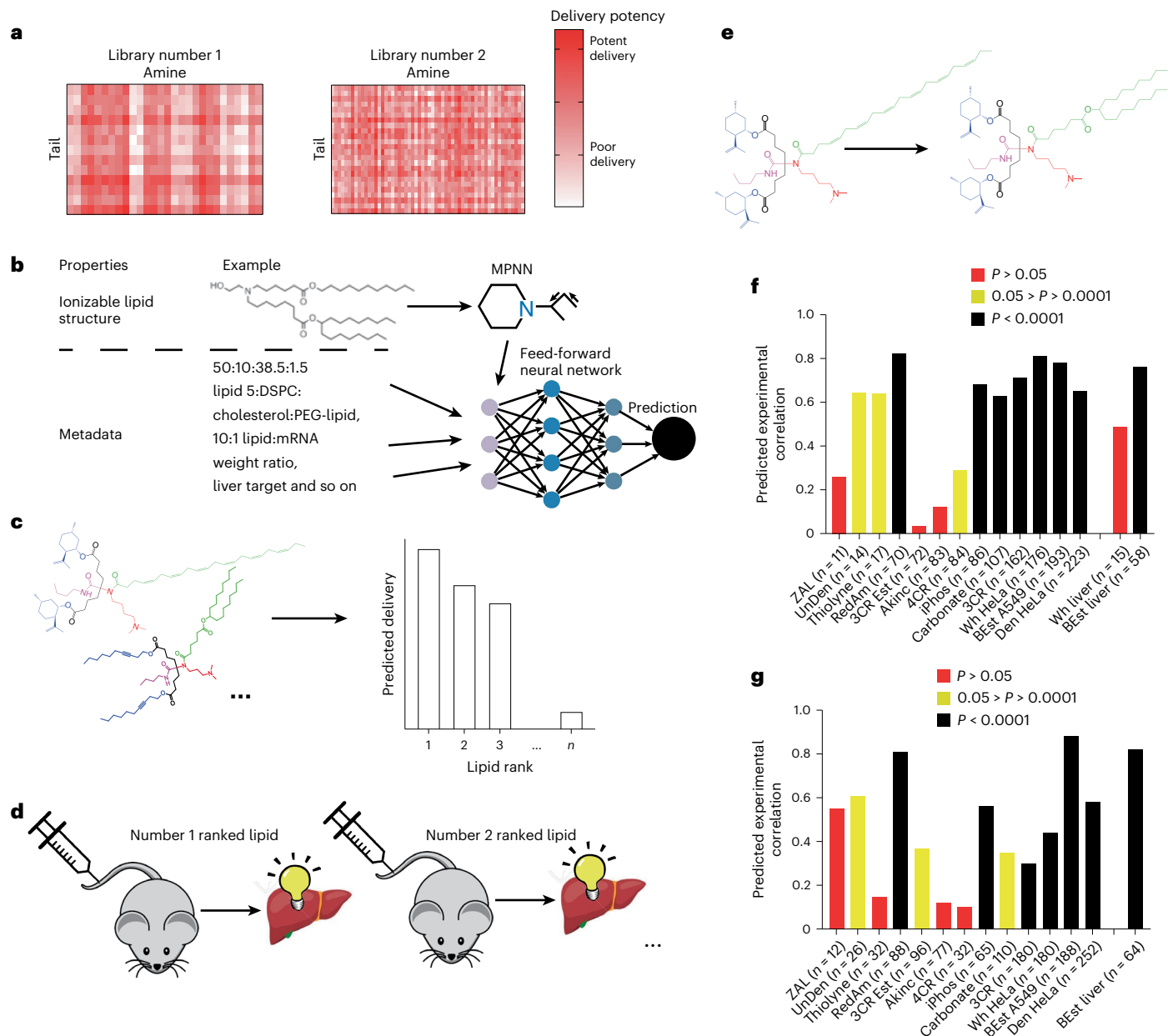


**Fig. 1 | Workflow for LiON, DL-based LNP design. a**, A collection of available LNP data, typically collected from a screen generated via combinatorial synthesis. **b**, Schematic of training of LiON, a predictive message-passing neural network (MPNN)-based DL model, on training data. The inputs are the chemical structure of the ionizable lipid along with metadata (formulation details, cargo and target of LNP). **c**, A ranking of lipids from a novel library using LiON. **d**, Top candidates are screened in vivo. **e**, Structural optimization of individual promising LNPs. **f, g**, Performance of LiON as measured by correlation between predicted and experimental delivery results on held-out test set using a random training–test

split (**f**) and an amine-based training–test split (**g**). Only datasets with  $n > 10$  in test set are shown. The  $P$  values for significance of correlation used a beta distribution for null hypothesis of no correlation and were two-sided. ZAL, zwitterionic amino lipids<sup>43</sup>; UnDen, unsaturated dendrimer lipids<sup>48</sup>; RedAm, reductive amination<sup>42</sup>; 3CR Est, three-component reaction with esters<sup>41</sup>; Akinc, lipids from Akinc et al.<sup>47</sup>; iPhos, ionizable phospholipids<sup>45</sup>; 3CR, three-component reaction<sup>15</sup>; Wh, Whitehead et al.<sup>27</sup>; BEst A549, branched ester lipids<sup>35</sup> tested in A549 cells; Den, dendrimer lipids<sup>44</sup>; BEst liver, branched ester lipids<sup>35</sup> tested in the liver.

RM-133-3 (Fig. 2f, g). Lastly, as a proof-of-concept protein replacement therapy applications, we tested delivery of erythropoietin (Epo) mRNA. RJ-A30-T01 performed at least comparably with lipid 5 and was ninefold better than RM-133-3 (Fig. 2h). A detailed characterization showed that RJ-A30-T01's expression was predominantly in the liver with minor spleen signal, the resulting LNPs could be freeze-thawed with minimal change in LNP diameter and the LNPs caused little detectable inflammation or liver damage (Supplementary Fig. 5).

RJ-A14-T34 had both a tail and headgroup that were not in the original 384-lipid screen, showing the model's ability to extrapolate. Also,

RJ-A30-T01 was in the original screen but was not identified as an assay positive, possibly due to nonlinear effects inherent to barcoded screening<sup>35</sup>. This shows that LiON can improve the results from barcoded screens.

To test whether the additional datasets included in the DL model improved performance over training on the barcoded branched-ester liver data alone, we trained a model only on the branched-ester liver dataset. This model ranked T01 and T34, the tails used in our two top candidates, in the bottom five (Supplementary Table 4). Hence, the incorporation of additional training datasets was required to identify RJ-A30-T01 and RJ-A14-T34. This highlights the importance of

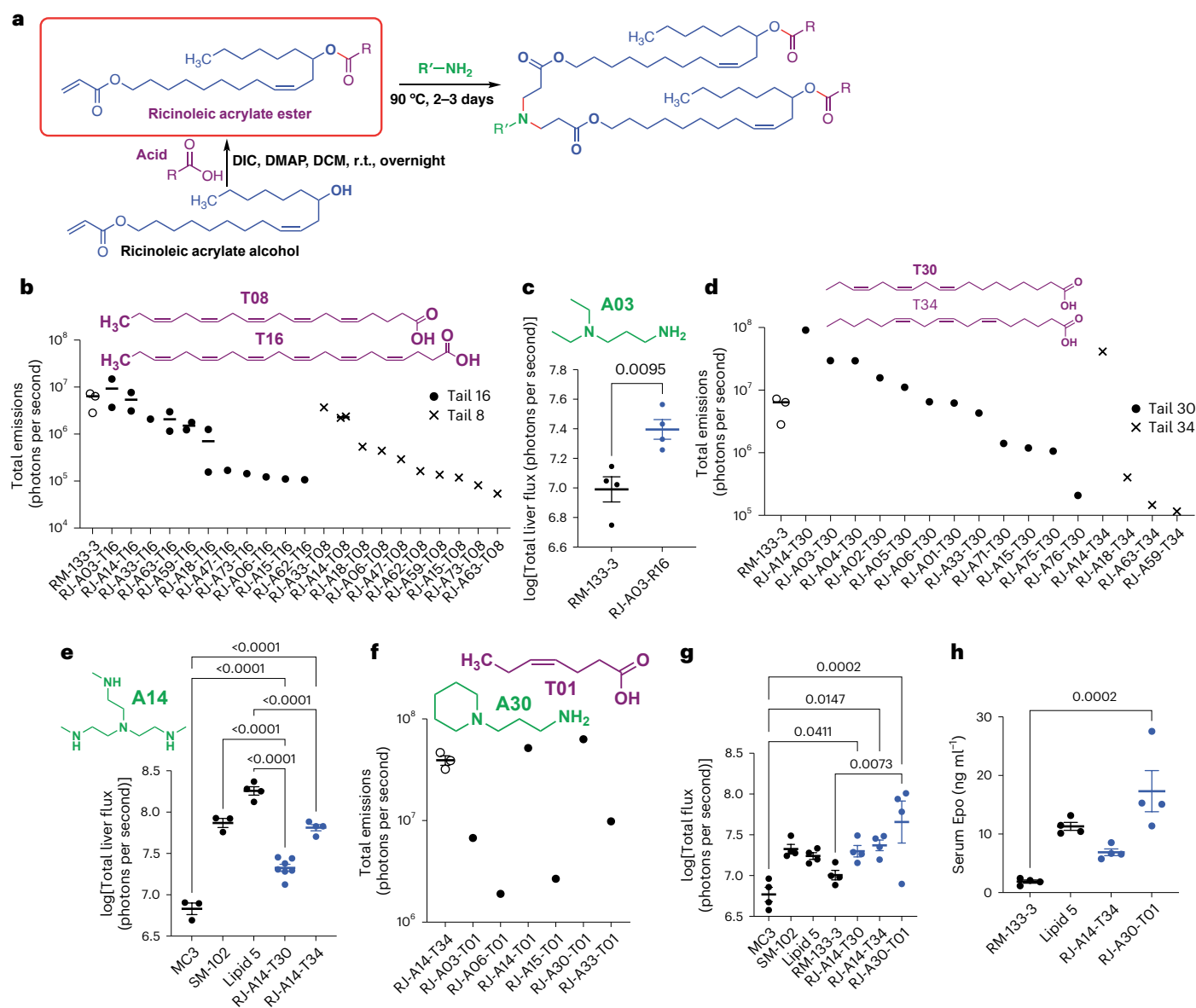


**Fig. 2** LiON for optimizing intravenous liver delivery of branched-ester-based library. **a**, Michael addition chemistry for generation of branched-tail ionizable lipids. DIC, *N,N'*-di(propan-2-yl)methanediimine; DMAP, 4-dimethylaminopyridine; DCM, dichloromethane; r.t., room temperature. **b**, A screen of top DL candidates with EPA (T08) and DHA (T16) tails.  $n = 3$  for RM-2-133-3 control,  $n = 1$  or 2 for the rest of the screen. **c**, RJ-A03-T16 has improved liver delivery compared with RM-133-3 (which, according to this work's nomenclature, would be designated RJ-A03-T08).  $n = 4$ ; unpaired *t*-test,  $t = 3.747$ , d.f. = 6. **d**, A screen of top DL candidates with ALA (T30) and GLA (T34) tails ( $n = 2$  for RM-133-3,  $n = 1$  otherwise). **e**, An evaluation of the top candidates

RJ-A14-T30 and RJ-A14-T34 relative to controls ( $n = 3$  or 4 for controls,  $n = 7$  for RJ-A14-T30,  $n = 4$  for RJ-A14-T34). **f**, A screening of candidates with tail T01, with RJ-A30-T01 as the top candidate ( $n = 3$  for RJ-A14-T34,  $n = 1$  otherwise). **g**, Testing of the top candidates relative to controls shows that RJ-A30-T01 appears to be the top performer ( $n = 4$ ). **h**, The serum Epo 6 h after Epo mRNA delivery ( $n = 4$ ). All doses are 1  $\mu\text{g}$ . For FFL mRNA delivery testing to the liver, 1  $\mu\text{g}$  dose is delivered intravenously, with imaging after 6 h. The error bars are the mean  $\pm$  s.e.m. One-way analysis of variances with Šidák's multiple comparisons test between controls (black) and novel lipids (blue) were performed for **e**, **g** and **h**. Exact *P* values of  $<0.05$  are shown for pairwise comparisons.

integrating multiple datasets and suggests that the usefulness of LiON will increase over time as more data become available and the model generalizes even more accurately.

### Application of LiON to a novel four-component library

**Design of lipids for intramuscular delivery.** While the ability to optimize existing screens is useful, it is more challenging (but potentially higher reward) to expand into novel, highly diverse chemical spaces. We, therefore, developed a four-component Ugi reaction between a primary amine, a carboxylic acid, an isocyanide and a ketone (Fig. 3a) and used LiON to suggest lipid structures. While related reactions have

been reported<sup>15,41,52</sup>, for this library, we had no data. Furthermore, the yield of this reaction was generally  $<10\%$ , so individual purification of lipids was required, precluding high-throughput testing. Despite these challenges, the 4CR offered substantial chemical diversity, so we used LiON to identify potent lipids.

To start, we ranked 86,400 lipids (Supplementary Fig. 6) by predicted delivery and selected the best-predicted candidates for in vivo testing. Because the training data for the closest analogs, the 3CR and 4CR reactions, were in HeLa cells using 35:16:46.5:2.5 lipid:DOPE:cholesterol:PEG-lipid molar ratios (referred to below as the 'KK' formulation<sup>53</sup>), we used these conditions as our metadata, as this produced the

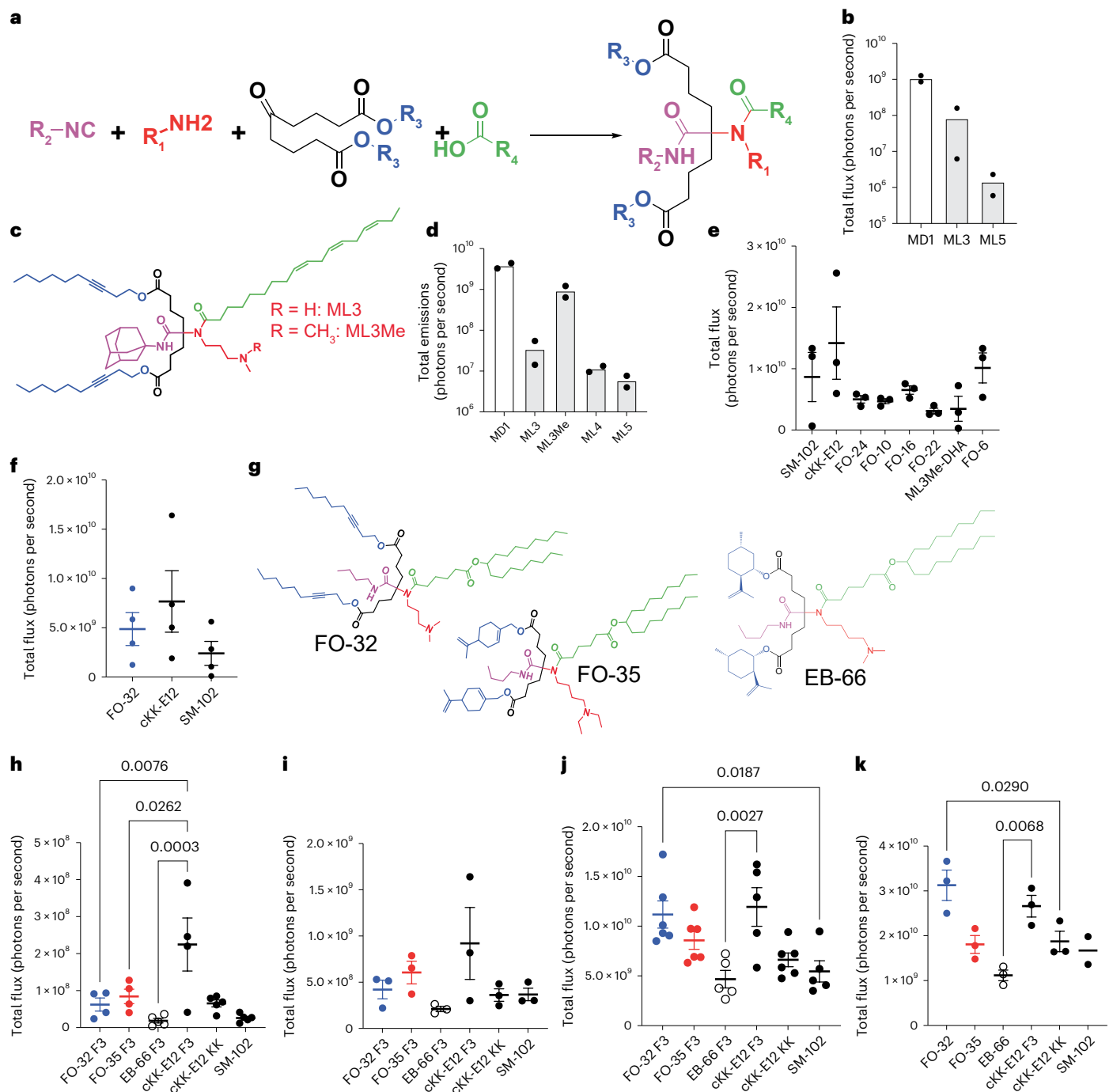


**Fig. 3 | Combining LiON with 4CR chemistry.** **a**, A 4CR scheme to generate novel ionizable lipids. **b**, Initial intramuscular (i.m.) delivery testing with ML3 and ML5 (1  $\mu\text{g}$  dose, BL/6 mice) compared with cKk-E12 ( $n = 1$  mouse per LNP injected on each flank). **c**, The structures of ML3 and ML3Me. **d**, Delivery of ML3Me is better than delivery of ML3 (1  $\mu\text{g}$  dose,  $n = 1$  mouse per LNP injected on each flank). **e**, Testing of top DL candidates against SM-102 and cKk-E12 controls (5  $\mu\text{g}$  dose,  $n = 3$ ) shows promise for some candidates. **f**, i.m. delivery of FO-32 compared with cKk-E12 and SM-102 (1  $\mu\text{g}$  dose,  $n = 4$ ). **g**, The structures of top candidates FO-32, FO-35 and EB-66. **h–k**, A comparison of delivery of formulation-optimized DL-

designed lipids compared with cKk-E12 (formulation matched and with original KK formulation) and SM-102 (clinical vaccine formulation), at 0.01  $\mu\text{g}$  ( $n = 4$ ) (**h**), 0.1  $\mu\text{g}$  ( $n = 3$ ) (**i**), 1  $\mu\text{g}$  ( $n = 5$  or 6) (**j**) and 10  $\mu\text{g}$  ( $n = 2$  or 3) (**k**) for SM-102 due to missed intraperitoneal (i.p.) injection doses. i.m. FFL mRNA delivery testing, imaged 6 h after injection in BALB/c mice unless otherwise indicated. The error bars are the mean  $\pm$  s.e.m. One-way analysis of variances with Šidák's multiple comparisons test between controls (cKk-E12 KK and F3 and SM-102) and novel lipids were performed for **h–k**. Exact  $P$  values of  $<0.05$  are shown for pairwise comparisons.

most stable predictions. We tested the resulting top predicted LNPs for intramuscular delivery, reasoning that a model trained mostly on in vitro delivery may predict local delivery better than systemic delivery. The first two candidates tested, ML3 and ML5, showed nonzero delivery potency (Fig. 3b and Supplementary Fig. 7) and also had

secondary ionizable amines, which is unusual for ionizable lipids. Converting ML3 to the tertiary amino analog ML3Me improved mRNA delivery (Fig. 3c,d), and carboxylic acid analogs of ML3Me yielded further improvement (Supplementary Fig. 8). Moving forward, we limited our possible amine headgroups to exclude secondary amines.

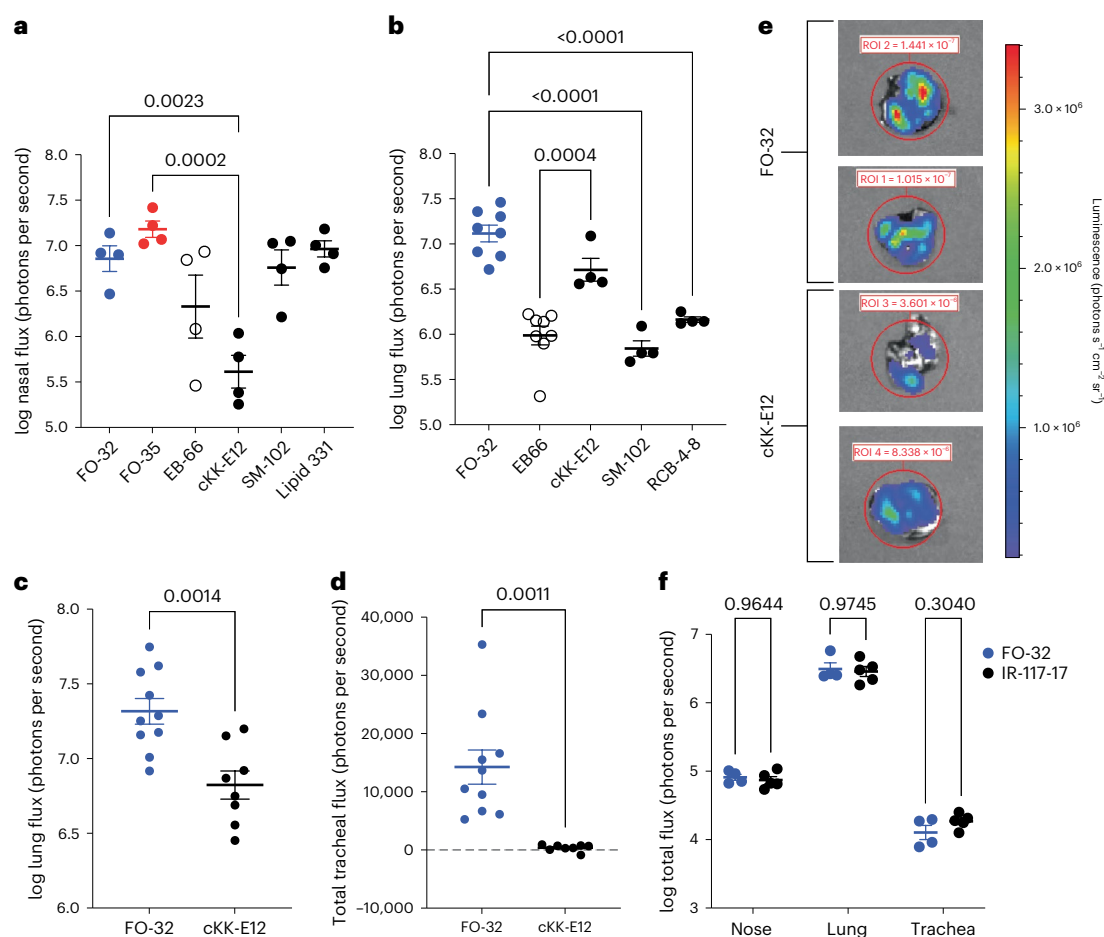


**Fig. 4 | Respiratory tract delivery. a**, IN FFL delivery (1.5  $\mu\text{g}$  dose,  $n = 4$ ) comparison between lead DL candidates (FO-32, FO-35 and EB-66) and controls (cKK-E12, SM-102 and lipid 331). **b**, OPA FFL delivery comparison (1  $\mu\text{g}$  dose,  $n = 8$  for novel LNPs,  $n = 4$  for controls) between lead LiON candidates and controls. One-way analysis of variances with Šidák's multiple comparisons test between controls (cKK-E12, SM-102, lipid 331 and RCB-4-8) and novel lipids were performed for **a** and **b**. **c, d**, OPA FFL delivery (1  $\mu\text{g}$  dose,  $n = 10$ , two outliers removed for cKK-E12 due to missed i.p. injections, two-sided Welch's  $t$ -test) for FO-32 compared with top control cKK-E12 for the lung luminescence (**c**) and tracheal luminescence (**d**) quantified following background subtraction due to

low signal. **e**, The representative lung image. ROI, luminescence over the region of interest. **f**, Nebulized FFL delivery (500  $\mu\text{g}$  dose,  $n = 5$ , two-way analysis of variance with Šidák's comparison test for IR-117-17 versus FO-32 in each tissue) for FO-32 compared with the top control IR-117-17 for nose, lung and trachea. Intranasal delivery is in BALB/c, and all OPA and nebulized testing was performed in BL/6 mice. The error bars are the mean  $\pm$  s.e.m. Outlier removal was based on the robust regression and outlier removal (ROUT) method ( $Q = 0.05$ ) and does not change any statistical significance. Exact  $P$  values of  $<0.05$  are shown for pairwise comparisons.

Next, *in silico* ranked lipids synthesizable from 53 amines, 60 carboxylic acids, 11 isocyanides and 51 ketones (Supplementary Table 5). Since the top several hundred lipids had essentially identical predictions, we hand-selected a set of chemically diverse lipids from the top 200 to synthesize and test. We also synthesized analogs of the top candidates, particularly *n*-butyl isocyanide analogs, which improved yield and dimethylaminopropylamine headgroups, as those were successful in previous Ugi lipids.

The results from the first round of testing are given in Supplementary Fig. 9, with follow-up testing shown in Fig. 3e. Many LNPs were of comparable transfection efficiency to SM-102, though lower than cKK-E12. The introduction of a branched carboxylic acid tail generated FO-32, which had comparable activity with both SM-102 and cKK-E12 (Fig. 3f,g and Supplementary Fig. 10). Systematic examination of FO-32 analogs did not yield further improvement (Supplementary Fig. 11).

Following formulation optimization via design of experiments (Supplementary Fig. 12 and Supplementary Tables 6 and 7) to identify formulation F3, we modified FO-16 and FO-22 to also contain branched carboxylic acid tails, resulting in FO-35 and EB-66 (Fig. 3g). We tested FO-32, FO-35 and EB-66 against cKK-E12 (formulated according to

F3 and KK formulations) and SM-102 across a broad range of doses (Fig. 3h-k and Supplementary Figs. 13 and 14). FO-32 and FO-35 were both more potent on average than cKK-E12 KK and SM-102 at every dose tested except for FO-35 at a high dose, though this difference was not always significant at each individual dose. At low doses, FO-35 was the most potent novel LNP, while at high doses, FO-32 was the most potent.

To better characterize the LNPs, we performed uptake,  $pK_a$ , inflammation and biodistribution studies. First, by treating with macropinocytosis inhibitor 5-(*N*-ethyl-*N*-isopropyl)amiloride and dynamin inhibitor dynasore<sup>54</sup>, we found that micropinocytosis but not dynamin-mediated internalization were critical for uptake of 4CR-based LNPs, similar to cKK-E12 but not SM-102 (Supplementary Fig. 15). Next, we found that while FO-32 LNPs had a  $pK_a$  of 6.36, well within typical optimal range (close to 6.5) for potency<sup>55</sup>, EB-66 ( $pK_a$  6.99) and especially FO-35 ( $pK_a$  7.67) were outside the typical range (Supplementary Fig. 16). LNP  $pK_a$  is hypothesized to affect endosomal escape during acidification<sup>55</sup>. How LNPs with a basic  $pK_a$  might facilitate delivery and endosomal escape will require further investigation. Lastly, we observed comparable inflammation and off-target systemic expression for all the LNPs we tested (Supplementary Fig. 17). Overall,

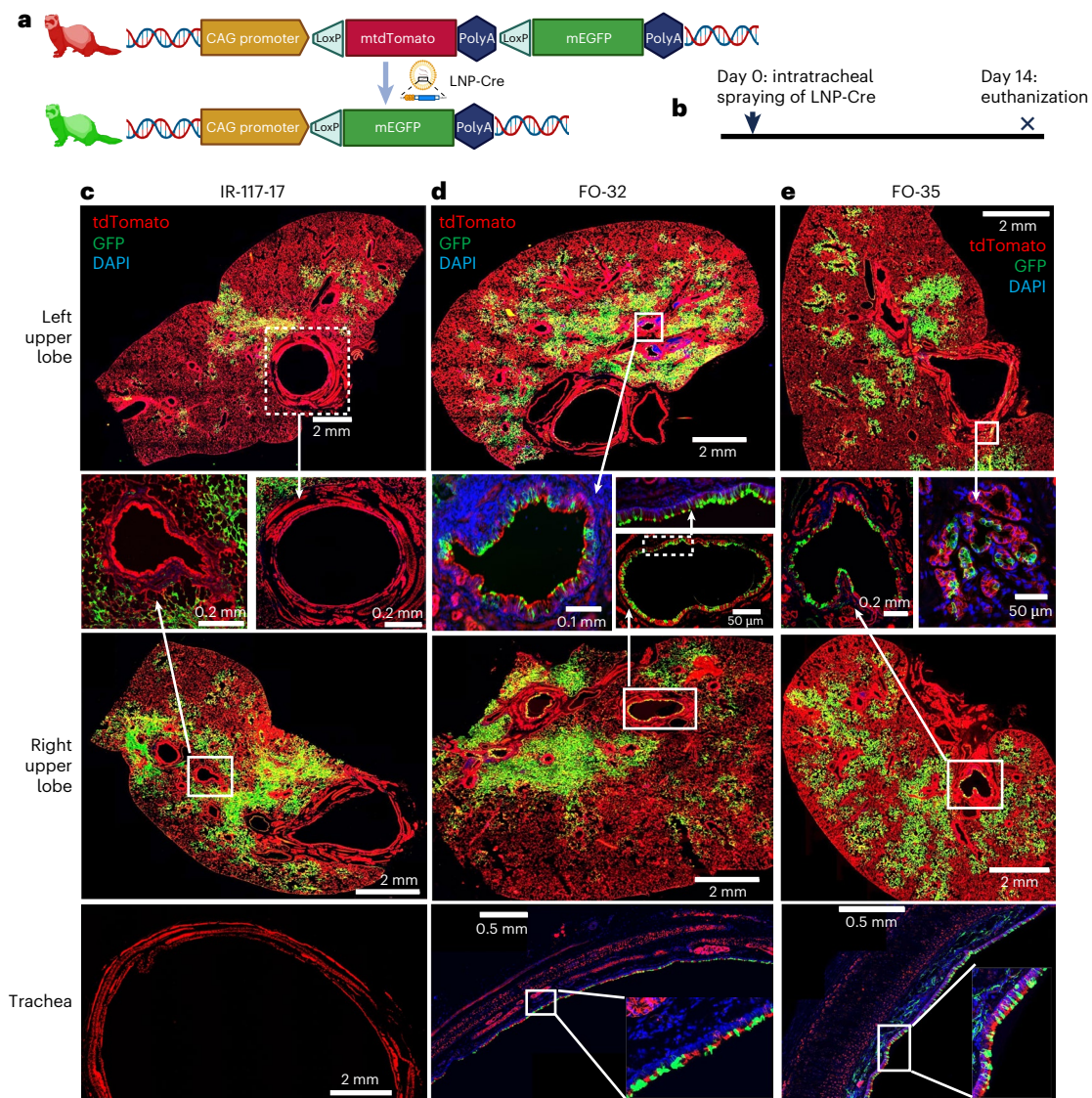


**Fig. 5 | LNP delivery testing in ferret model.** **a**, Ferret Cre reporter model. Cre activity converts cells from mtdTomato to mEGFP expression. **b**, The timeline of the LNP-Cre delivery experiments. **c–e**, Cre mRNA delivery to adult (>5 months old) ferret lungs (one ferret per LNP,  $0.6 \text{ mg kg}^{-1}$  total mRNA delivered in  $2 \text{ ml kg}^{-1}$  volume). The detailed manually selected images of highly transfected airways

show transfection of IR-117-17 (**c**), FO-32 (**d**) and FO-35 (**e**). For FO-35-treated ferret, the left upper lobe zoomed-in image shows transfection at the submucosal glands. The zoomed-out trachea for 117-17 shows undetectable transfection in the entire section. DAPI, 4',6-diamidino-2-phenylindole, a nuclear stain.

these results show great promise for intramuscular vaccination with FO-32 and FO-35.

**Lipid testing for respiratory tract delivery.** Next, we tested mRNA delivery to the respiratory tract. We first examined intranasal delivery of EB-66, FO-32 and FO-35 against the controls cKK-E12, SM-102 and lipid 331 (a recently published lipid used for intranasal vaccination<sup>41</sup>), using a formulation previously reported for intranasal vaccination<sup>41</sup>. FO-32 and FO-35 matched or exceeded all controls (Fig. 4a and Supplementary Fig. 18a) and, hence, are promising candidates for intranasal vaccines. Immediately after imaging for nasal delivery, we extracted the lungs and trachea of the mice, finding again that FO-32 and FO-35 matched or exceeded the delivery of the other lipids (Supplementary Fig. 18b–g). We also tested a 1,2-dioleoyl-3-trimethylammonium-propane (DOTAP)-free formulation to potentially minimize inflammation but observed sharply reduced transfection; in any case, no formulation caused substantial systemic expression or inflammation (Supplementary Fig. 19).

To further test delivery to the lower respiratory tract, we used oropharyngeal aspiration (OPA) with a previously reported nebulization-compatible formulation<sup>42</sup>. Consistent with the intranasal results, FO-32 had highly potent lung delivery while FO-35 was not far behind. FO-32 also had 2.5-fold, 13-fold, 9-fold and 6-fold better delivery than the control lipids cKK-E12, SM-102, RCB-4-8 (developed specifically for pulmonary mRNA delivery<sup>46</sup>) and IR-117-17 (also developed specifically for nebulized pulmonary mRNA delivery<sup>42</sup>), respectively (Fig. 4b and Supplementary Fig. 20a). Delivery to the trachea (a potentially valuable source of information regarding transfection of conducting airways) was noisier but broadly consistent with the intranasal and OPA results (Supplementary Fig. 20b,c). In a follow-up experiment testing FO-32 against the top control cKK-E12, we confirmed that FO-32 was threefold more potent than cKK-E12 in the lung and dramatically more potent in the trachea (Fig. 4c–e and Supplementary Fig. 20d). Our top LNPs retained activity, encapsulation efficiency and low size upon freeze–thaw (Supplementary Fig. 21), showing the potential for long-term shipping and storage. FO-32 also matched IR-117-17 for

**Table 1 | The percentage of GFP<sup>+</sup> cells out of the total number of bronchial epithelial cells in manually selected, highly transfected bronchi for each lobe, carina and trachea**

Lung section	FO-35	FO-32	IR-117-17
Carina	1.46	82.71	1.33
Trachea	39.55	31.21	1.72
Right upper lobe	36.3	69.6	0.28
Right middle lobe	1.76	63.77	2.27
Right lower lobe	4.18	81.55	1.81
Left upper lobe	4.69	58.5	0.8
Left lower lobe	22.98	18.43	1.34
Accessory lobe	2.12	79.48	1.71
Average	14.13	60.66	1.41

nebulized delivery using previously reported conditions that achieved state-of-the-art delivery with IR-117-17 (ref. 42) (Fig. 4f).

To test the translational potential of FO-32 and FO-35, we delivered Cre mRNA-loaded LNPs to Cre reporter ferret lungs via a tracheal micro-sprayer (Fig. 5a,b). We first confirmed that a 0.6 mg kg<sup>-1</sup> dose was well tolerated in juvenile ferrets and found that IR-117-17 formulated mRNA enabled delivery to the alveoli and terminal and respiratory bronchioles but not upper airways (Supplementary Figs. 22 and 23). Next, we treated adult ferrets with 0.6 mg kg<sup>-1</sup> of FO-32-, FO-35- and IR-117-17-based mRNA LNPs. Histology images of each lobe are depicted in Supplementary Fig. 24, and detailed images are depicted in Fig. 5c–e. All three LNPs transfected alveoli (Supplementary Fig. 25), but IR-117-17's transfection was confined to distal airways (Fig. 5c), while FO-32 and FO-35 expression were widespread throughout the airway tree (Fig. 5d,e). FO-35 transfection was even observed in submucosal glands (Fig. 5e), the key structures for CF and other airway diseases<sup>38,56,57</sup>. IR-117-17's contrast with FO-32 and FO-35 is interesting in light of its equal or better tracheal delivery in mice (Fig. 4f and Supplementary Fig. 20c), suggesting that despite the mouse trachea's utility as a conducting airway biology model<sup>58–60</sup> it may not be suited for predicting large animal gene therapy.

The whole-lung transfection quantification is complicated by uneven deposition over the lung using the micro-sprayer (since some airways would have zero transfection due to lack of locally deposited LNP), but the quantification of highly transfected bronchi was consistent with the qualitative impression, with potency in the order FO-32 ≥ FO-35 >> IR-117-17 (Table 1). This indicates translational potential of FO-32 and FO-35 for pulmonary gene therapy and/or gene editing.

**Lipid structural analysis.** Next, we tested how structurally unique our top lipids were. As measured by Tanimoto similarity<sup>61</sup>, FO-32 had the closest structural analog (Supplementary Fig. 26a(i)), and though this analog did not have an alkyne, alkynes were present in the dataset (Supplementary Fig. 26a(ii)) and have been reported to improve endosomal escape via increased fusogenicity<sup>62</sup>; FO-32 can, therefore, be thought of as combining groups identified in disparate screens to form a particularly potent lipid. However, alkyne tails performed poorly in vivo in our related three-component Ugi reaction library<sup>41</sup>, so this was a nonobvious combination. FO-35 and EB-66 were structurally unique, with lower Tanimoto similarity to the closest analog and no instances of their ketone tails in the training data (Supplementary Fig. 26b,c)—or, to our knowledge, in any publicly available ionizable lipid structure. It is possible that these bulky tails made the lipids more cone shaped, somewhat akin to branched tails. However, the nonobvious nature of these combined structures highlights the ability of LiON to identify unexpected structural elements that function synergistically. Precise mechanisms by which certain headgroup and tail combinations optimize function will require additional investigation.

**LiON 2.0: streamlining and cross validation.** Lastly, we updated LiON to incorporate cross validation, a more reliable approach than individual test-training splitting. LiON now reports results for fivefold cross validation (Supplementary Fig. 27) and makes predictions on new libraries by averaging over the trained five-model ensemble. The model and training data are available at [https://github.com/jswwitten/LNP\\_ML](https://github.com/jswwitten/LNP_ML) (ref. 63). Incorporation of additional datasets, model training, model performance analysis and predictions on new libraries can each be accomplished with a single command line prompt.

## Discussion

Here, we report two practical uses of DL for LNP design. First, we identified two branched-ester ionizable lipids, RJ-A30-T01 and RJ-A14-T34 with greatly improved activity over the lead compound from the branched-ester training set, RM-133-3. This is an important demonstration of DL's ability to identify functional molecules for complex tasks lacking a clear, structure-defined objective, such as protein binding<sup>64</sup>. DL on these complex tasks requires training data, which means that for DL to be useful, it must improve upon the top hits found in that training data. RJ-A30-T01 and RJ-A14-T34 cleared this hurdle and further showed that even the gold standard for LNP identification, barcoded in vivo screening, benefits from a DL-informed second pass.

Next, we used the 4CR chemistry to show that DL can extrapolate to new libraries to produce state-of-the-art lipids for mRNA delivery. This is another important result, as it demonstrates that in addition to being useful for secondary screens such as optimization of branched-ester lipids given an existing branched-ester dataset, LiON can design primary screens by prioritizing lipids to synthesize from a wholly new library.

Rational structure-activity relationship analysis has had success in the past<sup>27</sup>, so it is useful to consider its performance versus LiON. For the branched-ester library, because most of the hits from the prior screen had large tails, conventional SAR analysis focusing on the screen results would have been unlikely to identify RJ-A30-T01. For the 4CR library, incorporation of the branched-tail carboxylic acid shows the continued utility of rational design, but it seems unlikely that FO-35's unique perillyl alcohol tail would have been identified without LiON suggesting it. The combination of introduction of novel structures with LiON and human refinement, thus, points to a situation in which human-artificial intelligence collaboration outperforms either one separately as has been observed in other fields<sup>65</sup>.

More broadly, almost all top ionizable lipid tails so far have been variations on a similar theme: linear or branched alkanes, incorporating ester or disulfide bonds for degradability and with occasional unsaturation<sup>1,66</sup>. The main exceptions are cholesterol and fat-soluble vitamins<sup>67–70</sup>. We believe that this limited structural range is a consequence of basing ionizable lipid structures off lipids found in nature. LiON, by removing human bias and finding FO-35 and EB-66 with terpene (perillyl alcohol and isopulegol, respectively) tails, points the way toward unexplored classes of potent ionizable lipids.

FO-32 and FO-35's distinct mouse nose versus lung delivery and widespread ferret lung transfection (in comparison to IR-117-17's alveolar-directed transfection) illustrate another point: LiON can identify lipids with delivery potential, but performance in specific tissue settings must be verified experimentally. This reflects the largely in vitro training data, which carries no information about which organs will be targeted most effectively. Widespread multiorgan barcoded delivery data may help resolve this, though, as we show here, barcoded data have limitations. Single-LNP animal screening<sup>71</sup> provides helpful training data but is resource intensive, particularly for nonmouse models. In addition to high-throughput in vivo delivery data, high-throughput toxicity and immunogenicity measurements would also amplify LiON's usefulness by allowing for maximization of therapeutic index rather than potency alone.



The lead LNP formulations using FO-32 and FO-35 demonstrate considerable promise as candidates for intramuscular and intranasal vaccines, as well as for pulmonary gene therapy to treat difficult and deadly lung diseases<sup>14,72–74</sup>. The ferret pulmonary delivery is particularly important because, as we show here, results in mice may not translate to higher mammals; IR-117-17's efficient delivery in mice<sup>42</sup> translates to ferret alveoli but not to conducting airways important for muco-obstructive lung disease. Additionally, many lung diseases have at least some contribution from both alveolar and conducting airways<sup>75,76</sup>, so FO-32 and FO-35's whole-lung transfection could be useful for treating multiple relevant pathologies. Moving forward, we expect LiON and DL more broadly to generate many promising candidates for nanoparticle-based gene therapy.

## Online content

Any methods, additional references, Nature Portfolio reporting summaries, source data, extended data, supplementary information, acknowledgements, peer review information; details of author contributions and competing interests; and statements of data and code availability are available at <https://doi.org/10.1038/s41587-024-02490-y>.

## References

- Hou, X., Zaks, T., Langer, R. & Dong, Y. Lipid nanoparticles for mRNA delivery. *Nat. Rev. Mater.* **6**, 1078–1094 (2021).
- Barbier, A. J., Jiang, A. Y., Zhang, P., Wooster, R. & Anderson, D. G. The clinical progress of mRNA vaccines and immunotherapies. *Nat. Biotechnol.* **40**, 840–854 (2022).
- Witten, J., Hu, Y., Langer, R. & Anderson, D. G. Recent advances in nanoparticulate RNA delivery systems. *Proc. Natl Acad. Sci. USA* **121**, e2307798120 (2024).
- Polack, F. P. et al. Safety and efficacy of the BNT162b2 mRNA COVID-19 vaccine. *N. Engl. J. Med.* **383**, 2603–2615 (2020).
- Baden, L. R. et al. Efficacy and safety of the mRNA-1273 SARS-CoV-2 vaccine. *N. Engl. J. Med.* **384**, 403–416 (2021).
- Gillmore, J. D. et al. CRISPR–Cas9 in vivo gene editing for transthyretin amyloidosis. *N. Engl. J. Med.* **385**, 493–502 (2021).
- Rothgangl, T. et al. In vivo adenine base editing of PCSK9 in macaques reduces LDL cholesterol levels. *Nat. Biotechnol.* **39**, 949–957 (2021).
- Heymans, S. & Cooper, L. T. Myocarditis after COVID-19 mRNA vaccination: clinical observations and potential mechanisms. *Nat. Rev. Cardiol.* **19**, 75–77 (2022).
- vander Straeten, A. et al. A microneedle vaccine printer for thermostable COVID-19 mRNA vaccines. *Nat. Biotechnol.* **42**, 510–517 (2024).
- Muramatsu, H. et al. Lyophilization provides long-term stability for a lipid nanoparticle-formulated, nucleoside-modified mRNA vaccine. *Mol. Ther.* **30**, 1941–1951 (2022).
- Loughrey, D. & Dahlman, J. E. Non-liver mRNA delivery. *Acc. Chem. Res.* **55**, 13–23 (2022).
- Hodges, C. A. & Conlon, R. A. Delivering on the promise of gene editing for cystic fibrosis. *Genes Dis.* **6**, 97–108 (2018).
- Ensink, M., Mottais, A., Detry, C., Leal, T. & Carlon, M. S. On the corner of models and cure: gene editing in cystic fibrosis. *Front. Pharmacol.* **12**, 662110 (2021).
- Choi, S. H. & Engelhardt, J. F. Gene therapy for cystic fibrosis: lessons learned and paths forward. *Mol. Ther.* **29**, 428–430 (2021).
- Miao, L. et al. Delivery of mRNA vaccines with heterocyclic lipids increases anti-tumor efficacy by STING-mediated immune cell activation. *Nat. Biotechnol.* **37**, 1174–1185 (2019).
- Ruigrok, M. J. R., Frijlink, H. W., Melgert, B. N., Olinga, P. & Hinrichs, W. L. J. Gene therapy strategies for idiopathic pulmonary fibrosis: recent advances, current challenges, and future directions. *Mol. Ther. Methods Clin. Dev.* **20**, 483–496 (2021).
- Bai, X. et al. Inhaled siRNA nanoparticles targeting *IL11* inhibit lung fibrosis and improve pulmonary function post-bleomycin challenge. *Sci. Adv.* **8**, eabn7162 (2022).
- Zhang, R. et al. Inhaled mRNA nanoformulation with biogenic ribosomal protein reverses established pulmonary fibrosis in a bleomycin-induced murine model. *Adv. Mater.* **34**, e2107506 (2022).
- Guan, S., Darmstädter, M., Xu, C. & Rosenecker, J. In vitro investigations on optimizing and nebulization of IVT-mRNA formulations for potential pulmonary-based alpha-1-antitrypsin deficiency treatment. *Pharmaceutics* **13**, 1281 (2021).
- Wu, D.-D. et al. The potential for targeted rewriting of epigenetic marks in COPD as a new therapeutic approach. *Pharmacol. Ther.* **182**, 1–14 (2018).
- Woo, C. J. et al. Inhaled delivery of a lipid nanoparticle encapsulated messenger RNA encoding a ciliary protein for the treatment of primary ciliary dyskinesia. *Pulm. Pharmacol. Ther.* **75**, 102134 (2022).
- da Silva, A. L. et al. Nanoparticle-based thymulin gene therapy therapeutically reverses key pathology of experimental allergic asthma. *Sci. Adv.* **6**, eaay7973 (2020).
- Zeyer, F. et al. mRNA-mediated gene supplementation of Toll-like receptors as treatment strategy for asthma in vivo. *PLoS ONE* **11**, e0154001 (2016).
- Sabnis, S. et al. A novel amino lipid series for mRNA delivery: improved endosomal escape and sustained pharmacology and safety in non-human primates. *Mol. Ther.* **26**, 1509–1519 (2018).
- Hashiba, K. et al. Branching ionizable lipids can enhance the stability, fusogenicity, and functional delivery of mRNA. *Small Sci.* **3**, 2370001 (2023).
- Lam, K. et al. Unsaturated, trialkyl ionizable lipids are versatile LNP components for therapeutic and vaccine applications. *Adv. Mater.* **35**, 2209624 (2023).
- Whitehead, K. A. et al. Degradable lipid nanoparticles with predictable in vivo siRNA delivery activity. *Nat. Commun.* **5**, 4277 (2014).
- Li, B. et al. Accelerating ionizable lipid discovery for mRNA delivery using machine learning and combinatorial chemistry. *Nat. Mater.* **23**, 1002–1008 (2024).
- Stokes, J. M. et al. A deep learning approach to antibiotic discovery. *Cell* **180**, 688–702.e13 (2020).
- Yang, K. et al. Analyzing learned molecular representations for property prediction. *J. Chem. Inf. Model.* **59**, 3370–3388 (2019).
- Soleimany, A. P. et al. Evidential deep learning for guided molecular property prediction and discovery. *ACS Cent. Sci.* **7**, 1356–1367 (2021).
- Reker, D. et al. Computationally guided high-throughput design of self-assembling drug nanoparticles. *Nat. Nanotechnol.* **16**, 725–733 (2021).
- Liu, G. et al. Deep learning-guided discovery of an antibiotic targeting *Acinetobacter baumannii*. *Nat. Chem. Biol.* **19**, 1342–1350 (2023).
- Wong, F. et al. Discovery of a structural class of antibiotics with explainable deep learning. *Nature* **626**, 177–185 (2024).
- Rhym, L. H., Manan, R. S., Koller, A., Stephanie, G. & Anderson, D. G. Peptide-encoding mRNA barcodes for the high-throughput in vivo screening of libraries of lipid nanoparticles for mRNA delivery. *Nat. Biomed. Eng.* **7**, 901–910 (2023).
- Ryan, K. A. et al. Dose-dependent response to infection with SARS-CoV-2 in the ferret model and evidence of protective immunity. *Nat. Commun.* **12**, 81 (2021).
- Rosen, B. H. et al. Animal and model systems for studying cystic fibrosis. *J. Cyst. Fibros.* **17**, S28–S34 (2018).
- Yuan, F. et al. Transgenic ferret models define pulmonary ionocyte diversity and function. *Nature* **621**, 857–867 (2023).

39. Rotolo, L. et al. Species-agnostic polymeric formulations for inhalable messenger RNA delivery to the lung. *Nat. Mater.* **22**, 369–379 (2023).
40. Boucher, R. C. Muco-obstructive lung diseases. *N. Engl. J. Med.* **380**, 1941–1953 (2019).
41. Li, B. et al. Enhancing the immunogenicity of lipid-nanoparticle mRNA vaccines by adjuvanting the ionizable lipid and the mRNA. *Nat. Biomed. Eng.* <https://doi.org/10.1038/s41551-023-01082-6> (2023).
42. Jiang, A. Y. et al. Combinatorial development of nebulized mRNA delivery formulations for the lungs. *Nat. Nanotechnol.* **19**, 364–375 (2024).
43. Miller, J. B. et al. Non-viral CRISPR/Cas gene editing in vitro and in vivo enabled by synthetic nanoparticle co-delivery of Cas9 mRNA and sgRNA. *Angew. Chem. Int. Ed.* **56**, 1059–1063 (2017).
44. Zhou, K. et al. Modular degradable dendrimers enable small RNAs to extend survival in an aggressive liver cancer model. *Proc. Natl Acad. Sci. USA* **113**, 520–525 (2016).
45. Liu, S. et al. Membrane-destabilizing ionizable phospholipids for organ-selective mRNA delivery and CRISPR–Cas gene editing. *Nat. Mater.* **20**, 701–710 (2021).
46. Li, B. et al. Combinatorial design of nanoparticles for pulmonary mRNA delivery and genome editing. *Nat. Biotechnol.* **41**, 1410–1415 (2023).
47. Akinc, A. et al. A combinatorial library of lipid-like materials for delivery of RNAi therapeutics. *Nat. Biotechnol.* **26**, 561–569 (2008).
48. Lee, S. M. et al. A systematic study of unsaturation in lipid nanoparticles leads to improved mRNA transfection in vivo. *Angew. Chem.* **133**, 5912–5917 (2021).
49. Li, L. et al. A biomimetic lipid library for gene delivery through thiol-yne click chemistry. *Biomaterials* **33**, 8160–8166 (2012).
50. Heid, E. et al. Chemprop: a machine learning package for chemical property prediction. *J. Chem. Inf. Model.* **64**, 9–17 (2024).
51. Wu, Z. et al. MoleculeNet: a benchmark for molecular machine learning. *Chem. Sci.* **9**, 513–530 (2018).
52. He, Z. et al. A multidimensional approach to modulating ionizable lipids for high-performing and organ-selective mRNA delivery. *Angew. Chem. Int. Ed.* **62**, e202310401 (2023).
53. Kauffman, K. J. et al. Optimization of lipid nanoparticle formulations for mRNA delivery in vivo with fractional factorial and definitive screening designs. *Nano Lett.* **15**, 7300–7306 (2015).
54. Gilleron, J. et al. Image-based analysis of lipid nanoparticle-mediated siRNA delivery, intracellular trafficking and endosomal escape. *Nat. Biotechnol.* **31**, 638–646 (2013).
55. Carrasco, M. J. et al. Ionization and structural properties of mRNA lipid nanoparticles influence expression in intramuscular and intravascular administration. *Commun. Biol.* **4**, 956 (2021).
56. Fischer, A. J. et al. Mucus strands from submucosal glands initiate mucociliary transport of large particles. *JCI Insight* **4**, e124863 (2019).
57. Ostedgaard, L. S. et al. Lack of airway submucosal glands impairs respiratory host defenses. *eLife* **9**, e59653 (2020).
58. Tata, P. R. & Rajagopal, J. Plasticity in the lung: making and breaking cell identity. *Development* **144**, 755–766 (2017).
59. Plasschaert, L. W. et al. A single-cell atlas of the airway epithelium reveals the CFTR-rich pulmonary ionocyte. *Nature* **560**, 377–381 (2018).
60. Shah, V. S., Chivukula, R. R., Lin, B., Waghray, A. & Rajagopal, J. Cystic fibrosis and the cells of the airway epithelium: what are ionocytes and what do they do? *Annu. Rev. Pathol. Mech. Dis.* **17**, 23–46 (2022).
61. Bajusz, D., Rácz, A. & Héberger, K. Why is Tanimoto index an appropriate choice for fingerprint-based similarity calculations? *J. Cheminform.* **7**, 20 (2015).
62. Miao, L. et al. Synergistic lipid compositions for albumin receptor mediated delivery of mRNA to the liver. *Nat. Commun.* **11**, 2424 (2020).
63. Witten, J. & Collins, E. LNP ML. *GitHub* [https://github.com/jswitten/LNP\\_ML](https://github.com/jswitten/LNP_ML) (2024).
64. Guo, Z. et al. Diffusion models in bioinformatics and computational biology. *Nat. Rev. Bioeng.* **2**, 136–154 (2024).
65. Reverberi, C. et al. Experimental evidence of effective human–AI collaboration in medical decision-making. *Sci. Rep.* **12**, 14952 (2022).
66. Xu, Y., Golubovic, A., Xu, S., Pan, A. & Li, B. Rational design and combinatorial chemistry of ionizable lipids for RNA delivery. *J. Mater. Chem. B* **11**, 6527–6539 (2023).
67. Du, S. et al. Cholesterol-amino-phosphate (CAP) derived lipid nanoparticles for delivery of self-amplifying RNA and restoration of spermatogenesis in infertile mice. *Adv. Sci.* **10**, 2300188 (2023).
68. Andries, O. et al. Comparison of the gene transfer efficiency of mRNA/GL67 and pDNA/GL67 complexes in respiratory cells. *Mol. Pharm.* **9**, 2136–2145 (2012).
69. Hou, X. et al. Vitamin lipid nanoparticles enable adoptive macrophage transfer for the treatment of multidrug-resistant bacterial sepsis. *Nat. Nanotechnol.* **15**, 41–46 (2020).
70. Oyama, R. et al. An ionizable lipid material with a vitamin E scaffold as an mRNA vaccine platform for efficient cytotoxic T cell responses. *ACS Nano* **17**, 18758–18774 (2023).
71. Goldman, R. L. et al. Understanding structure activity relationships of good HEPES lipids for lipid nanoparticle mRNA vaccine applications. *Biomaterials* **301**, 122243 (2023).
72. Yan, Z., McCray, P. B. Jr & Engelhardt, J. F. Advances in gene therapy for cystic fibrosis lung disease. *Hum. Mol. Genet.* **28**, R88–R94 (2019).
73. Lee, J.-A. et al. Gene therapy for cystic fibrosis: new tools for precision medicine. *J. Transl. Med.* **19**, 452 (2021).
74. Boucher, R. C. Status of gene therapy for cystic fibrosis lung disease. *J. Clin. Invest.* **103**, 441–445 (1999).
75. Ulrich, M. et al. Alveolar inflammation in cystic fibrosis. *J. Cyst. Fibros.* **9**, 217–227 (2010).
76. Lin, C.-R., Bahmed, K. & Kosmider, B. Impaired alveolar re-epithelialization in pulmonary emphysema. *Cells* **11**, 2055 (2022).

**Publisher's note** Springer Nature remains neutral with regard to jurisdictional claims in published maps and institutional affiliations.

Springer Nature or its licensor (e.g. a society or other partner) holds exclusive rights to this article under a publishing agreement with the author(s) or other rightsholder(s); author self-archiving of the accepted manuscript version of this article is solely governed by the terms of such publishing agreement and applicable law.

© The Author(s), under exclusive licence to Springer Nature America, Inc. 2024

## Methods

### Chemical synthesis of 4CR lipids

All reagents and solvents were purchased commercially unless noted otherwise. The amine and ketone were dissolved in dichloromethane and agitated at room temperature for 1 h. Then, the carboxylic acid was dissolved in methanol and added to the reaction vessel followed by a subsequently addition of the isocyanide. The four reactants were combined in an equimolar fashion. Dichloromethane and methanol were used at a volumetric ratio of 2:1. After addition of all four components, the reaction was agitated at room temperature for a minimum of 5 days. The solvent was removed via rotary evaporation before purification. Flash chromatography was performed on an ISCO CombiFlash Lumen instrument using ISCO RediSep Flash Cartridges. The ionizable lipids were purified using a solvent system of dichloromethane and methanol with 0.1% ammonium hydroxide (10:1 volumetric ratio). The product was collected, and the solvent was removed. The final compounds were confirmed via mass spectrometry and  $^1\text{H}$  nuclear magnetic resonance (NMR). Because the yield of the reactions was typically low (<10%), two (and occasionally three) successive CombiFlash purifications were often required to generate pure product. Mass spectrometry was performed using a high-resolution Agilent 6545 mass spectrometer coupled to an Agilent Infinity 1260 liquid chromatography system. Spectra collection was performed with the ionizable lipid sample dissolved in liquid chromatography–mass spectrometry grade methanol.  $^1\text{H}$  NMR was performed using a three-channel Bruker Advance Neo spectrometer operating at 400.17 MHz. The spectra collection was performed with the ionizable lipid sample dissolved in deuterated chloroform. Top performing lipids after screening (FO-32, FO-35 and EB-66) were fully characterized by NMR.

### Isocyanide intermediate synthesis for 4CR lipids

All isocyanides, with the exception of oleyl isocyanide, were purchased commercially. The synthesis of the oleyl isocyanide is described in detail in Supplementary Information.

### Ketone intermediate synthesis for 4CR lipids

Ketone intermediates were synthesized following the procedure reported in Li et al.<sup>41</sup>

### Carboxylic acid intermediate synthesis for 4CR lipids

The carboxylic acids were synthesized using Sterglich esterification. The dicarboxylic acid, alkyl alcohol, *N*-(3-dimethylaminopropyl)-*N'*-ethylcarbodiimide hydrochloride, 4-(dimethylamino) pyridine and *N,N*-diisopropylethylamine were combined at molar ratios of 1:1:1.5:0.5:2, respectively. The reaction was carried out at room temperature in dichloromethane for 24 h. The solvent was removed via rotary evaporation before purification. Flash chromatography was performed on an ISCO CombiFlash Lumen instrument using ISCO RediSep Flash Cartridges. The ionizable lipids were purified using a solvent system of dichloromethane and methanol (10:1 volumetric ratio). The product was collected and the solvent was removed.

### Chemical synthesis of branched-ester lipids

The branched-ester lipids were synthesized as previously reported<sup>35</sup> and further details are provided in Supplementary Information. Ricinoleic acid intermediates and top-performing lipids after screening (RJ-A30-T01) were fully characterized by NMR.

### A549 formulation screen

The A549 cells were plated in 384-well white plates (2,000 cells per well) and left to grow overnight. The next day, LNPs were hand-mixed with the appropriate formulation and ionizable lipid, and the cells were treated with 20 ng of FFL mRNA per well ( $n = 3$  wells per LNP). The cells and LNPs were incubated overnight and luminescence was read the next day using Bright-Glo (Promega). The results of this screen can be

found in Supplementary Information in rows with 'Experiment\_ID' = 'A549\_form\_screen'. Each row contains formulation parameters, ionizable lipid SMILES and log luminescence.

### Data collection

To collect data available in the literature, we wrote code to translate colors from heat maps to delivery potency as specified by the color scheme in the relevant publication. Supplementary Fig. 28 shows representative heat maps, with the dots showing the locations from which the colors were measured, confirming that we are drawing from the correct pixels to interpret delivery. We also routinely checked each scraped heat map to see that randomly selected good and bad transfection candidates were assigned to the correct lipid. We also algorithmically generated the SMILES form of each chemical structure based on the input components for each ionizable lipid. For the only literature-collected dataset not available in heat map form, the Den Liver dataset<sup>44</sup>, we used the in vivo data in Fig. 3b by classifying each lipid (discarding the generation two and above dendrimers) by relative factor VII activity, discretizing by the scale at the top of the plot as being in ranges [0,0.25], [0.25, 0.5], [0.5, 0.75] and [0.75, 1].

While collecting the data, we assumed that datapoints are directly comparable within individual screens but not necessarily between different screens or testing modalities. To avoid overemphasis on any one dataset, we log-transformed luminescence measurements that varied over multiple orders of magnitude and standardized each differently measured dataset to have mean 0 and standard deviation 1.

### DL model

We used Chemprop<sup>50</sup>, a Python package built for DL on molecular structures. The metadata (formulation, target and so on) were included as 'custom features'. Where hyperparameter optimization was specified, we used the built-in grid search with 20 possible hyperparameter sets; our optimized parameters were set to: depth of 4, dropout of 0.1, three feedforward network layers and hidden layer sizes of 600 networks. For the model trained only on the size 384 screen, the optimized parameters were: depth of 4, dropout of 0, three feedforward network layer and hidden layer sizes of 300 networks. For a given training–validation–test split, the models were trained five separate times, and the overall prediction was the average over this ensemble.

### LNP synthesis

LNPs for the branched-ester work were synthesized by mixing an aqueous phase containing the mRNA with an ethanol phase containing the lipids in a microfluidic chip device<sup>77</sup>. The aqueous phase was prepared in a 10 mM citrate buffer with corresponding mRNA (provided by Sanofi). The ethanol phase was prepared by solubilizing a mixture of ionizable lipid, DOPE, cholesterol and 1,2-dimyristoyl-*sn*-glycero-3-phosphoethanolamine-*N*-(methoxy(polyethylene glycol)-2000) ( $\text{C}_{14}$ -PEG<sub>2000</sub>), at mass ratios of 72.3:7.8:15.6:4.2 ionizable lipid:DOPE:cholesterol: $\text{C}_{14}$ -PEG<sub>2000</sub> and a 20:1 ionizable lipid:mRNA weight ratio<sup>35</sup>. To prepare the ethanol phase, ionizable lipids insoluble at a 20 mg ml<sup>-1</sup> stock concentration were heated until soluble, up to -60–70 °C, and then added to the rest of the ethanol phase. Additionally, for insoluble lipids, the complete ethanol phase was kept heated to 37 °C until immediately before LNP synthesis. The aqueous and ethanol phases were mixed at a 3:1 ratio by syringe pumps to a final mRNA concentration of 0.05 mg ml<sup>-1</sup>. Despite these measures, LNPs generated from lipids with greater than or equal to four tails were still noticeably cloudy.

For the 4CR experiments, all  $n = 1$  intramuscular screening was done with hand-mixed undialyzed LNPs, and all other testing was done with microfluidic synthesis. The KK formulation was 35:16:46.5:2.5 ionizable lipid:DOPE:cholesterol: $\text{C}_{14}$ -PEG<sub>2000</sub>, and formulation F3 was 25:15:58.5:1.5 ionizable lipid:DOPE:cholesterol: $\text{C}_{14}$ -PEG<sub>2000</sub>. Intranasal experiments used a 30:39:30:1 ionizable lipid:DOTAP:cholesterol: $\text{C}_{14}$ -PEG<sub>2000</sub> formulation. Nebulization and OPA experiments used the T1-5 formulation

(35:28:34.5:2.5 ionizable lipid:DOTAP:cholesterol:C<sub>14</sub>-PEG<sub>2000</sub>, using a nominal ionizable lipid molecular weight of C12-200, 1,137 g mol<sup>-1</sup>)<sup>42</sup>. All 4CR formulations used a 10:1 ionizable lipid:mRNA weight ratio.

SM-102, MC3 and lipid 5 controls were formulated according to 50:10:38.5:1.5 ionizable lipid:distearoylphosphatidylcholine (DSPC):cholesterol:C<sub>14</sub>-PEG<sub>2000</sub>.

All helper lipids were from Avanti Polar Lipids.

Microfluidically synthesized LNPs were dialyzed against PBS, in a 10,000 molecular weight cut-off (MWCO) Pierce 96-well microdialysis plate (ThermoFisher) or 20,000 MWCO dialysis cassette (ThermoFisher). For the nebulization experiment, following a 4-h dialysis in PBS, LNPs were dialyzed in 100 mM sodium acetate buffer overnight and nebulized with 2% w/v branched PEG20K acrylate (Sigma)<sup>42</sup>.

The LNPs were concentrated using 100,000 MWCO centrifugation filters (Sigma or ThermoFisher) at 4 °C. Total RNA and encapsulation efficiencies were measured using a Ribogreen assay (ThermoFisher).

For the Cre reporter experiments and freeze–thaw testing, LNPs were synthesized, dialyzed and concentrated, and the aliquots were flash-frozen in liquid nitrogen with 5% sucrose cryoprotectant. The aliquots were shipped in dry ice for testing.

### In vivo luciferase and Epo testing

For liver-targeted luminescence testing, C57BL/6 mice were injected intravenously with LNPs encapsulating FFL mRNA. For intranasal delivery, 15 µl per mouse was delivered to anesthetized mice. OPA administration was performed as previously described to deliver 50 µl of LNPs<sup>78</sup>. Specifically, mice were anesthetized and then hung up on a wire by their top teeth. Their tongues were pulled out and 25 µl of LNPs were pipetted to the back of the throat. After several breaths to make sure those 25 µl were inhaled, another 25 µl were administered.

To image luminescence, 200 µl per mouse of Xenolight D-luciferin (20 mg ml<sup>-1</sup> solution in Dulbecco's phosphate-buffered saline (DPBS); PerkinElmer) was injected to each mouse through intraperitoneal injection 6 h after LNP administration. To image mice following intravenous, intranasal or OPA administration, the mice were killed 8–9 min after intraperitoneal injection. The relevant organs were collected and imaged under Xenogen in vivo imaging system. The total flux (photons per second) of bioluminescence in each organ was quantified. For nasal imaging, the mice were imaged while anesthetized and before euthanasia. For intramuscular injection, the mice were imaged while anesthetized and not killed.

For Epo testing, C57BL/6 mice were injected intravenously with LNPs encapsulating Epo mRNA. A total of 6 and 24 h after injection, the serum was collected and assayed for human Epo using an ELISA (Abcam, product ab274397).

The nebulization experiment was conducted as previously described using a whole-body nebulization chamber and a vibrating mesh nebulizer<sup>42</sup>. Specifically, mice were placed in a nebulization chamber (adapted from a standard mouse anesthesia chamber) and LNPs were placed in a vibrating mesh nebulizer (Aeroneb Lab Nebulizer Unit, Small VMD). The aerosolized LNPs were connected via a tee junction to the nebulization chamber and oxygen at 15 feet<sup>3</sup> h<sup>-1</sup> was used to blow aerosol into the chamber. Nebulization was performed until aerosol was no longer being made.

All procedures were performed under an animal protocol approved by the Massachusetts Institute of Technology Committee on Animal Care and the guidelines for animal care in an Massachusetts Institute of Technology animal facility.

### Inflammatory and toxicity measurements

The serum was collected via submandibular blood collection and measured for cytokine levels by Eve Technologies and for alanine aminotransferase (ALT) and aspartate transaminase (AST) by the Massachusetts Institute of Technology Division of Comparative Medicine Diagnostic Lab.

### Nanoparticle characterization

For pK<sub>a</sub> measurements, a total of 16 buffers ranging from pH values of 2 to 11 were prepared using 100 mM stocks of citric acid, sodium monobasic phosphate and sodium bicarbonate. A stock solution of 6-(*p*-toluidino)-2-naphthalenesulfonic acid sodium salt (TNS) in water was prepared at 150 µM, and the LNPs were prepared at 100 ng µl<sup>-1</sup> mRNA concentrations. In a black 96-well plate, 88 µl of buffer, 10 µl of LNP and 2 µl of TNS were added in each well. The TNS fluorescence of each well was measured, and the half maximal point of the resulting fluorescence was calculated as the LNP pK<sub>a</sub>.

The size was measured using a Wyatt Dyna Pro Plate Reader Dynamic Light Scattering instrument.

### Flow cytometry

A total of 10,000 HeLa cells per well were plated and allowed to grow overnight. The next day, the HeLa cells were incubated with Dil-labeled LNPs for 4 h, then detached by washing with 1× PBS and treatment by 0.25% trypsin–EDTA buffer for 5 min. The cells were then stained by eFluor 780 Live/Dead (Invitrogen 65-0865-14) in 1× PBS for 30 min at 4 °C, before washing by 1× PBS two times and overnight fixation by 0.5% paraformaldehyde in 1× PBS. The cells were resuspended in 1× PBS containing 5% FBS and then analyzed by a FACSymphony A3 flow cytometer (BD Biosciences). The Dil dye and eFluor 780 dye were analyzed by excitation at 561 and 640 nm, respectively. The Dil-labeled LNPs were formulated with 0.5 mol% Dil with cholesterol content reduced by 0.5 mol% to compensate. The data were analyzed using FlowJo v10.10.0.

### Ferret Cre reporter testing

The ROSA-TG ferret model used in this test harbors a CRE-recombinase-responsive reporter cassette 'CAG promoter-LoxP-(m)tdTomato-STOP-loxP-(m)eGFP' integrated within the ROSA locus. This cassette expresses a membrane-bound tdTomato reporter. Upon introduction of CRE expression in the recipient cells, a conversion of red to green fluorescence occurs due to the excision of the 'tdTomato-STOP' element, which consequentially leads to the expression of membrane-bound enhanced green fluorescent protein (eGFP) reporter<sup>79</sup>. The 2-month-old juvenile ROSA-TG ferrets were used to test the low (150 ng µl<sup>-1</sup> total RNA concentration) and high dose (300 ng µl<sup>-1</sup> total RNA concentration) of IR-117-17 LNP-Cre mRNA. The 1–2-year-old adult ROSA-TG ferrets were used to test the FO-32, FO-35 and IR-117-17 Cre mRNA LNPs. The doses were intratracheally administered with LNP-Cre mRNA using a spray atomizer at a volume of 2 ml kg<sup>-1</sup> (refs. 80,81). Lung and tracheal tissue from these ferrets were collected 2 weeks after administration, fixed with 4% PFA and embedded in OCT for dissection. The slides were observed with a Leica DM68 microscope. The GFP cell turnover rate of the whole epithelial cell on the bronchial airway was quantified using Fiji version 2.9.0. All ferret experimentation was performed according to protocols approved by the Institutional Animal Care and Use committees of the University of Iowa.

### Statisticals and reproducibility

Statistical analysis was conducted using GraphPad Prism 9, except for Fig. 1f,g, which used the `scipy.stats.pearsonr` function. Multiple comparisons were performed between each new artificial intelligence-designed lipid, and each control lipid, that is, cKK-E12 and SM-102 were not compared with each other. All tests were two-sided. For zoomed-in images of airway transfection, due to uneven LNP deposition, it was not possible to identify fully representative images, so whole-lobe images were searched for transfected locations that were used for figures.

### Reporting summary

Further information on research design is available in the Nature Portfolio Reporting Summary linked to this article.

## Data availability

All code and data used for training models can be found at GitHub via [https://github.com/jswitten/LNP\\_ML](https://github.com/jswitten/LNP_ML) (ref. 63). Source data are provided with this paper.

## Code availability

All code and data used for training models can be found at GitHub via [https://github.com/jswitten/LNP\\_ML](https://github.com/jswitten/LNP_ML) (ref. 63).

## References

77. Chen, D. et al. Rapid discovery of potent siRNA-containing lipid nanoparticles enabled by controlled microfluidic formulation. *J. Am. Chem. Soc.* **134**, 6948–6951 (2012).
78. Ferguson, L. T. et al. Mechanisms by which liposomes improve inhaled drug delivery for alveolar diseases. *Adv. NanoBiomed Res.* **3**, 2200106 (2023).
79. Yu, M. et al. Highly efficient transgenesis in ferrets using CRISPR/Cas9-mediated homology-independent insertion at the *ROSA26* locus. *Sci. Rep.* **9**, 1971 (2019).
80. Tang, Y. et al. Repeat dosing of AAV2.5T to ferret lungs elicits an antibody response that diminishes transduction in an age-dependent manner. *Mol. Ther. Methods Clin. Dev.* **19**, 186–200 (2020).
81. Tang, Y. et al. Immunosuppression reduces rAAV2.5T neutralizing antibodies that limit efficacy following repeat dosing to ferret lungs. *Mol. Ther. Methods Clin. Dev.* **29**, 70–80 (2023).

## Acknowledgements

This work was supported by Sanofi and the National Institutes of Health (grant no. HL162564-02 and R61AI161805 to D.G.A. and grants no. HL152960, DK054759 and 75N92019C00010 to J.F.E.). It was also funded in part by a grant from the Alpha-1 Foundation. J.W. was supported by the Cystic Fibrosis Foundation awards WITTEN19XX0 and 004831F5222 and the Convergence Scholars Program through the Marble Center for Cancer Nanomedicine. This work was supported in part by the Koch Institute support grant 5P30-CA14051 from the National Cancer Institute. We thank the Koch Institute's Robert A. Swanson (1969) Biotechnology Center for technical

support, specifically the Animal Imaging and Preclinical Testing, Flow Cytometry, and Peterson (1957) Nanotechnology Materials core facilities.

## Author contributions

J.W., I.R., R.S.M., E.B., S.B., Y.T., M.E., J.L., D.N., F.O., A.Y.J., E.M., Y.H., H.M., A.S., E.C., Z.Y. and J.F.E. performed experiments and analyzed data. J.W., R.L. and D.G.A. discussed the results and wrote the paper with input from all authors. R.L. and D.G.A. acquired funding and supervised the project. J.W., I.R. and R.S.M. contributed equally and all reserve the right to list themselves first on their curricula vitae (CVs).

## Competing interests

J.W., I.R. and D.G.A. have filed a patent for the 4CR ketone biodegradable lipid library described herein and J.W., R.S.M. and D.G.A. have filed a patent for the branched-ester library described herein. Z.Y. and J.F.E. are consultants for Spirovant Sciences. D.G.A. receives research funding from Sanofi/Translate Bio and is a Founder of oRNA Tx. R.L. is a co-founder and board of director of Moderna. He also serves on the board and has equity in Particles For Humanity. For a list of entities with which R.L. is, or has been recently involved compensated or uncompensated, see <https://www.dropbox.com/s/yc3xqb5s8s94v7x/Rev%20Langer%20COI.pdf?dl=0>. The other authors declare no competing interests.

## Additional information

**Supplementary information** The online version contains supplementary material available at <https://doi.org/10.1038/s41587-024-02490-y>.

**Correspondence and requests for materials** should be addressed to Daniel G. Anderson.

**Peer review information** *Nature Biotechnology* thanks Yizhou Dong, Ho Lun Wong and the other, anonymous, reviewer(s) for their contribution to the peer review of this work.

**Reprints and permissions information** is available at [www.nature.com/reprints](http://www.nature.com/reprints).

## Reporting Summary

Nature Portfolio wishes to improve the reproducibility of the work that we publish. This form provides structure for consistency and transparency in reporting. For further information on Nature Portfolio policies, see our [Editorial Policies](#) and the [Editorial Policy Checklist](#).

### Statistics

For all statistical analyses, confirm that the following items are present in the figure legend, table legend, main text, or Methods section.

n/a Confirmed

- The exact sample size ( $n$ ) for each experimental group/condition, given as a discrete number and unit of measurement
- A statement on whether measurements were taken from distinct samples or whether the same sample was measured repeatedly
- The statistical test(s) used AND whether they are one- or two-sided  
*Only common tests should be described solely by name; describe more complex techniques in the Methods section.*
- A description of all covariates tested
- A description of any assumptions or corrections, such as tests of normality and adjustment for multiple comparisons
- A full description of the statistical parameters including central tendency (e.g. means) or other basic estimates (e.g. regression coefficient) AND variation (e.g. standard deviation) or associated estimates of uncertainty (e.g. confidence intervals)
- For null hypothesis testing, the test statistic (e.g.  $F$ ,  $t$ ,  $r$ ) with confidence intervals, effect sizes, degrees of freedom and  $P$  value noted  
*Give  $P$  values as exact values whenever suitable.*
- For Bayesian analysis, information on the choice of priors and Markov chain Monte Carlo settings
- For hierarchical and complex designs, identification of the appropriate level for tests and full reporting of outcomes
- Estimates of effect sizes (e.g. Cohen's  $d$ , Pearson's  $r$ ), indicating how they were calculated

*Our web collection on [statistics for biologists](#) contains articles on many of the points above.*

### Software and code

Policy information about [availability of computer code](#)

Data collection In vivo data was collected using a Xenogen in vivo imaging system. Flow cytometry was performed using a FACSymphony A3 flow cytometer (BD Biosciences, USA). Size was measured using a Wyatt Dyna Pro Plate Reader Dynamic Light Scattering instrument.

Data analysis Data was analyzed using GraphPad Prism 9. Information on the machine learning model can be found at [https://github.com/jswitten/LNP\\_ML](https://github.com/jswitten/LNP_ML). Flow cytometry data was analyzed using FlowJo v10.10.0 and ferret histology images were analyzed using Fiji version 2.9.0.

For manuscripts utilizing custom algorithms or software that are central to the research but not yet described in published literature, software must be made available to editors and reviewers. We strongly encourage code deposition in a community repository (e.g. GitHub). See the Nature Portfolio [guidelines for submitting code & software](#) for further information.

### Data

Policy information about [availability of data](#)

All manuscripts must include a [data availability statement](#). This statement should provide the following information, where applicable:

- Accession codes, unique identifiers, or web links for publicly available datasets
- A description of any restrictions on data availability
- For clinical datasets or third party data, please ensure that the statement adheres to our [policy](#)

All data used for training models can be found at [https://github.com/jswitten/LNP\\_ML](https://github.com/jswitten/LNP_ML). All quantitative data used for plots in figures is available in the Source Data file.

## Research involving human participants, their data, or biological material

Policy information about studies with [human participants or human data](#). See also policy information about [sex, gender \(identity/presentation\), and sexual orientation](#) and [race, ethnicity and racism](#).

Reporting on sex and gender	n/a
Reporting on race, ethnicity, or other socially relevant groupings	n/a
Population characteristics	n/a
Recruitment	n/a
Ethics oversight	n/a

Note that full information on the approval of the study protocol must also be provided in the manuscript.

## Field-specific reporting

Please select the one below that is the best fit for your research. If you are not sure, read the appropriate sections before making your selection.

Life sciences       Behavioural & social sciences       Ecological, evolutionary & environmental sciences

For a reference copy of the document with all sections, see [nature.com/documents/nr-reporting-summary-flat.pdf](https://nature.com/documents/nr-reporting-summary-flat.pdf)

## Life sciences study design

All studies must disclose on these points even when the disclosure is negative.

Sample size	Sample sizes were determined based on our previous experience with in vivo LNP studies to balance power with minimizing animal usage. For screens, n=1 was used to maximize throughput with occasional n=2 or 3 to check for consistency. For testing, we used n=4-5 as this has been used in the past to good success (see for example our work on nebulized LNPs, <a href="https://doi.org/10.1038/s41565-023-01548-3">https://doi.org/10.1038/s41565-023-01548-3</a> ). We used n=10 for Figure 4C-E to maximize power for increased confidence in our results.
Data exclusions	Four datapoints were excluded, one for SM-102 in Figure 3K, two for cKK-E12 in Figure 4C, and one for FO-32 in Figure 4F because the luminescence values were 2 orders of magnitude lower than the other values. In our experience this is usually due to an improper IP injection of luciferin. Because these were controls, incorporating these datapoints would have made our novel LNPs look even better by comparison, with the exception of Figure 4F, but in all cases statistical significance was not affected. Thus, this does not affect the conclusions of the study. Raw data including excluded data is provided in Source Data.
Replication	The overall performance of RJ-A30-T01 was verified independently using luciferase and epo mRNA. The performance of 4CR lipids intramuscularly was tested across 4 different doses, each providing independent confirmation of excellent potency via IM delivery. The performance of FO-32 via intratracheal delivery was confirmed via a large follow-up replication (Figure 4C).
Randomization	Organisms and other study materials (such as wells for in vitro testing) were all put randomly into different groups.
Blinding	Investigators were not blinded during analysis because one of the the lead authors (JW) performed all of the in vivo mouse studies. Thus, blinding was not logistically feasible.

## Reporting for specific materials, systems and methods

We require information from authors about some types of materials, experimental systems and methods used in many studies. Here, indicate whether each material, system or method listed is relevant to your study. If you are not sure if a list item applies to your research, read the appropriate section before selecting a response.

## Materials &amp; experimental systems

## Methods

- n/a  Involved in the study
- Antibodies
- Eukaryotic cell lines
- Palaeontology and archaeology
- Animals and other organisms
- Clinical data
- Dual use research of concern
- Plants

- n/a  Involved in the study
- ChIP-seq
- Flow cytometry
- MRI-based neuroimaging

## Eukaryotic cell lines

Policy information about [cell lines and Sex and Gender in Research](#)

Cell line source(s)	HeLa cells, A549 cells, both from ATCC.
Authentication	HeLa and A549 cells were not authenticated
Mycoplasma contamination	Neither HeLa nor A549 cells were tested for mycoplasma contamination
Commonly misidentified lines (See <a href="#">ICLAC</a> register)	HeLa cells generally contaminate other cell lines, not the other way around. A549 cells had the expected morphology.

## Animals and other research organisms

Policy information about [studies involving animals](#); [ARRIVE guidelines](#) recommended for reporting animal research, and [Sex and Gender in Research](#)

Laboratory animals	The study used 6-9w mice (BALB/C and BL/6) or adult (>5 month old) ferrets
Wild animals	No wild animals were used in this study.
Reporting on sex	Mouse experiments used female mice as is standard in the field as these are easier to handle. Strong sex dependence of LNP transfection have not been observed and no reproductive organs were targeted.
Field-collected samples	No field-collected samples were used in this study.
Ethics oversight	All procedures were performed under an animal protocol approved by the Massachusetts Institute of Technology Committee on Animal Care (mouse studies) or the Institutional Animal Care and Use committees of the University of Iowa (ferret studies).

Note that full information on the approval of the study protocol must also be provided in the manuscript.

## Plants

Seed stocks	n/a
Novel plant genotypes	n/a
Authentication	n/a



## Plots

Confirm that:

- The axis labels state the marker and fluorochrome used (e.g. CD4-FITC).
- The axis scales are clearly visible. Include numbers along axes only for bottom left plot of group (a 'group' is an analysis of identical markers).
- All plots are contour plots with outliers or pseudocolor plots.
- A numerical value for number of cells or percentage (with statistics) is provided.

## Methodology

Sample preparation

10,000 HeLa cells/well were plated and allowed to grow overnight. The next day, HeLa cells were incubated with Dil-labeled LNPs for 4 h, then detached by washing with 1x PBS and treatment by 0.25% trypsin-EDTA for 5 min. The cells were then stained by eFluor 780 Live/Dead (Invitrogen 65-0865-14) in 1x PBS for 30 min at 4°C, before washing by 1x PBS for 2 times and overnight fixation by 0.5% paraformaldehyde in 1x PBS. The cells were resuspended in 1x PBS containing 5% FBS and then analyzed by a FACSymphony A3 flow cytometer (BD Biosciences, USA).

Instrument

FACSymphony A3 flow cytometer (BD Biosciences, USA)

Software

FlowJo

Cell population abundance

The flow cytometry experiment was carried out on a cancer cell line (HeLa) cultured in vitro. All cells that were seeded into each well from each treatment group were collected for staining and analysis, therefore there is no ambiguity on cell abundance from each treatment group.

Gating strategy

HeLa cells were gated using FSC-A/SSC-A to exclude debris from cells, for which debris were defined as points with a reading of FSC-A below ~40K. The cells were further gated by FSC-A/FSC-W to select singlets, and then subjected to gating on viability for which viable cells are defined as those with a reading of eFluor 780 below ~2000. The Dil intensity of viable cells were then analyzed on a histogram, with a Dil-positive gate defined by applying a gate until the Dil-positive frequency of a negative control group reached below 0.1%. An example of the gating strategy is shown in Supplementary Information.

- Tick this box to confirm that a figure exemplifying the gating strategy is provided in the Supplementary Information.